CrossMark

Effects of chelating agents on the performance of Li$_{1.2}$Mn$_{0.54}$Ni$_{0.13}$Co$_{0.13}$O$_2$ as cathode material for Li-ion battery prepared by sol–gel method

Qing Wu[1] · Li Zhao[1] · Jinzhu Wu[2]

Abstract In this study, Li$_{1.2}$Mn$_{0.54}$Ni$_{0.13}$Co$_{0.13}$O$_2$ as lithium-ion battery cathode active material was prepared by a sol–gel method. The effects of chelating agents including three different kinds of chelating agents (citric acid, glycolic acid, and polyvinyl pyrrolidone) on its performance were studied. X-ray diffraction tests were carried out to explore the samples' structure, showing α-NaFeO$_2$ structure with $R - \overline{3}m$ space group for all the samples. After various kinds of tests, the sample prepared with citric acid showed the worst properties among the three samples. The sample prepared with polyvinyl pyrrolidone has the smallest size (200–350 nm), with uniform distribution and smooth surfaces. Electrochemical tests show that it has the highest initial discharge capacity (231 mAh g^{-1}) and initial charge/discharge efficiency (70.9%). Electrical impedance spectroscopy confirms that its low charge-transfer resistance is responsible for the superior discharge capacity and rate performance. Furthermore, the sample prepared with polyvinyl pyrrolidone could improve its cycle performance after coating with 3% graphene; its capacity retention is up to 89.8% after 100 cycles at 1 C rate. The sample prepared with glycolic acid achieved the best cycling stability. The discharge capacity was decreased from 150 to 138 mAh g^{-1}, and the capacity retention rate was as high as 91.7% after 100th cycle under a current of 1 C.

Graphical Abstract

Chelating agent: PS-PVP, GS-Glycolic acid, CS- Citric acid
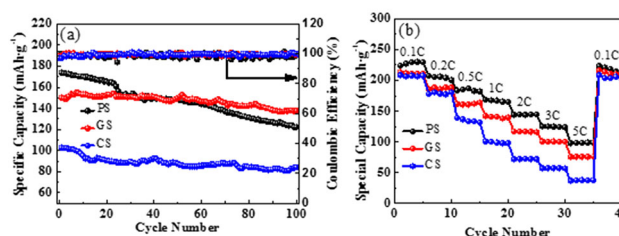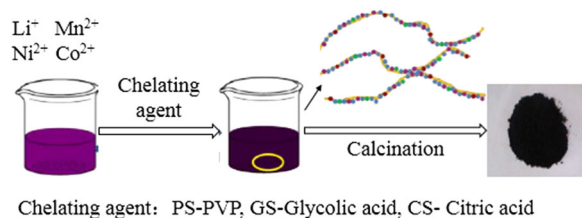
✉ Li Zhao
dhx907@hit.edu.cn

1 MIIT Key Laboratory of Critical Materials Technology for New Energy Conversion and Storage, School of Chemistry and Chemical Engineering, Harbin Institute of Technology, Harbin 150001, People's Republic of China

2 Department of Materials Chemistry, School of Chemistry and Chemical Engineering, Harbin Institute of Technology, Harbin 150001, People's Republic of China

1 Introduction

Lithium-ion batteries have been widely used because of their advantages such as high-working voltage, high energy density, excellent rate performance, safety, long cycle life, low self-discharge, and no memory effect [1]. However, drawbacks [2] such as large first charge–discharge irreversible capacity loss, instability at high-voltage cycle, and

Springer

high cost of $LiCoO_2$ limited their applications. Preparation of cathode materials with low price, high capacity, and good stability becomes the current research direction.

Mn-based Li-rich material as cathode material for lithium-ion batteries was the research focus referring to layered Li_2MnO_3, and layered $LiMO_2$ (M=Ni, Co, Mn) formed a solid solution [3]. First proposed by Numata [4] in 1997, Li-rich material attracted widespread concern for its high capacity and stable cycle characteristics. Compared with conventional layered cathode material, Mn-based Li-rich material, $xLi_2MnO_3 \cdot (1-x)LiMO_2$ (M=Ni, Co, Mn) [5], contains a certain amount of lithium in transition metal layer. Thinking from the perspective of defect chemistry, incorporation with the excess amount of lithium prevents from forming vacancies due to Li volatilization and from making the excess lithium into interstitial lattice to form a solid solution. Although it showed excellent electrochemical performance, its poor circulation performance and low first coulombic efficiency cannot be ignored, which can be improved by doping with metal ions such as Mg, K, Fe, Sn, Zn, Zr, etc. [6–11] or coated with C, Al_2O_3, CeO_2, and fluoride [12–16]. The doped metal ions may generally maintain the structure stability of the material to promote circulation performance, and surface coating could prevent the direct contact of the active substance with the electrolytic solution to avoid the decomposition of the electrolytic solution. Recently, hollow microspheric active material that can improve the rate capability and cycle performance was synthesized, as the hollow sphere increases the surface area and shortens Li^+ migration path, stabilizing material microstructure [17].

Many methods have been used to synthesize Mn-based Li-rich materials, such as solid phase sintering method [18], sol–gel method [19], combustion method [20], hydrothermal method [21], and co-precipitation method [22]. The sol–gel method is to use a highly active compound as a precursor, together with raw materials to form a liquid phase and then be subjected to hydrolysis and condensation to generate a stable transparent sol system. The resulting gel network is filled with the solvent without fluidity, which was then calcinated to produce nanomaterials. The sol–gel method has many advantages; for instance, it can achieve the molecular-level mixing of the raw materials and precursors, it requires relatively low-temperature treatment, small and narrow diameter distribution of products can be produced, simple equipment and easy operation are needed and so on [23]. Chelating agents have effects on the performance of the synthesized materials. In this work, Li-rich material, $Li_{1.2}Mn_{0.54}Ni_{0.13}Co_{0.13}O_2$, was prepared by a sol–gel method using different chelating agents. The effects of the chelating agents on the structure and electrochemical performance of the materials were investigated.

2 Experiment

2.1 Preparation of materials

All the chemicals used in this work were of analytical grade and with no further purification. The cathode material $Li_{1.2}Mn_{0.54}Ni_{0.13}Co_{0.13}O_2$ was synthesized by the sol–gel method using different chemical compounds as a chelating agent. A stoichiometric amount of $Ni(CH_3COO)_2 \cdot 4H_2O$, $Co(CH_3COO)_2 \cdot 4H_2O$, $Mn(CH_3COO)_2 \cdot 4H_2O$, and $LiCH_3COO \cdot H_2O$ was dissolved in distilled water with 5% excess of $LiCH_3COO$; the solution was labeled as A in which total cation concentration was $2\,mol\,L^{-1}$. An amount of chelating agent was dissolved in distilled water, and the solution was labeled as B. Solution B was added dropwise into stirring solution A. Thereafter, the pH value of the solution was adjusted using ammonia water, and the solution was evaporated under continuous stirring at 90 °C until the viscidity maroon aquogel was formed. After drying at 120 °C in a drying oven overnight, the xerogel was crushed, subsequently heated at 450 °C for 5 h in air to decompose the organic constituents and acetate components. The sample was then grounded, pelletized, and calcined at 900 °C for 12 h followed by grounding for later use as the temperature cooled down to room temperature. In this study, citric acid, glycolic acid, and polyvinyl pyrrolidone (PVP, K30) were used as chelating agents, and the corresponding samples were labeled as CS, GS and PS, respectively.

2.2 Performance measurements

All the samples were characterized using X-ray diffraction (XRD, Rigaku Ultima D/max-RB 12 KW) with a Cu Kα radiation source. Data were collected in the range 10–90° at a scanning rate of $5°\,min^{-1}$. Morphological studies on the samples were performed using a Hitachi SU8010 scanning electron microscope (SEM).

Electrochemical measurements were performed using galvanostatic cycling with two-electrode coin-cells (type CR2025). The sample: acetylene black: PVDF = 8:1:1 with an appropriate amount of N-Methyl-2-pyrrolidone (NMP) was ground to a uniform syrupy substance. After the slurry was uniformly coated on aluminum foil, it was moved into the vacuum drying oven and then formed into electrode sheets. In a glove box filled with argon, metallic lithium was used as the negative electrode sheets with the prepared sheets as cathode to assemble CR2025 button cell. The electrolyte used $1\,M$ $LiPF_6$ in EC:DEC (1:1). Constant current charge–discharge cycle test was carried out on battery test system at room temperature; the voltage range was 2.0–4.8 V.

A CHI electrochemical workstation (CHI660e, Shanghai, China) was used to perform cyclic voltammograms (CV) of

the prepared materials between 2.0 and 4.8 V at a sweep rate of $0.1\ \mathrm{mV\ s^{-1}}$ at room temperature. A two-electrode system will be used to conduct the Electrochemical Impedance Spectra (EIS) of the cells in which the working electrode is cathode and the reference and the auxiliary electrode is lithium anode by the CHI660e electrochemical workstation before charge and discharge at frequencies from 10 MHz to 0.01 Hz with an AC perturbation signal of 5 mV. The EIS was analyzed using the Zsimpwin software. The potentials throughout the paper are referenced to the $\mathrm{Li^+/Li}$ couple.

3 Results and discussion

3.1 Characterization of $Li_{1.2}Mn_{0.54}Ni_{0.13}Co_{0.13}O_2$

Figure 1 shows the XRD pattern of the samples synthesized with different chelating agents. The lattice parameters of the samples are calculated and presented in Table 1. It can be seen from Fig. 1 that the diffraction peaks are sharp, indicating the well crystallinity of the samples. All peaks can be indexed to PDF-#20-1115 showing a α-$NaFeO_2$ structure with $R-\overline{3}m$ space group. The well-separated diffraction peaks of (006)/(012) and (108)/(110) demonstrate the layered structure of the synthesized lithium-rich material [24]. The values of c/a and $I_{(003)}/I_{(104)}$ generally are indicative of the ordering and the cation mixing degree of the layered structure, respectively [25, 26]. From Table 1, the c/a values of the composites were all larger than 4.899, indicating that the materials have a better layered structure. The PS sample has a largest c/a value among the three samples, which illustrates that this sample has a good rate performance. The $I_{(003)}/I_{(104)}$ values of the synthesized materials were all greater than 1.2, meaning less cationic mixing, which means that the cationic mixing of CS sample is the smallest. The c value represents the distance between Li_2O layer and MO layer. It can be seen from Table 1 that

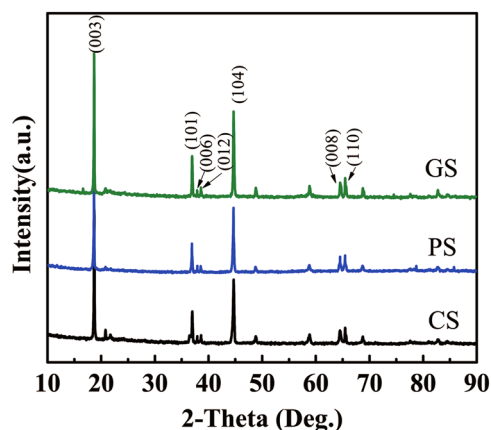the c-axis of the material changes slightly with different chelating agents. The PS sample with a larger distance between Li_2O layer and MO layer leads to easier intercalation of Li-ions, which could result in high discharge capacity. Dahn [27] found that R-factor ($R = (I_{(006)} + I_{(012)})/I_{(101)}$) could be used to measure the structural order of the layered material—the lower the value, the higher the order of the material that possesses better electrochemical performance. Considering the R-factor in Table 1, the sample prepared with citric acid has the highest R value, which means that its electrochemical performance may be the worst. Meanwhile, the values of the sample prepared with glycolic acid and PVP are almost the same.

The morphology and size of the samples have certain influence on the electrochemical performance. Small particle size will lead to a better rate performance. When the material is in nanoscale, the diffusion path for Li-ions' migration is greatly reduced, resulting in the increased carrier de-embedding and improved high-current discharge performance. Figure 2 shows SEM images of materials synthesized with different chelating agents. It can be seen that different chelating agents have little effects on the dispersibility of the particles. The particle size of the material with citric acid is the largest, whereas the particle size of the material with PVP is the smallest, indicating that macromolecular chelating agent can reduce the particle sizes. As a result, the large-rate performance of the material with PVP could be better than that of the other two materials.

3.2 Electrochemical performance

Studies on the de-/insertion Li-ions process of the lithium-rich materials reveal that the potential vs. Li^+/Li value of lower than 4.5 V indicates that the reaction accords with the traditional lithium-ion deintercalation theory; that is, Li^+ deintercalating from $Li_{1.2}Mn_{0.54}Ni_{0.13}Co_{0.13}O_2$ lattice follows Ni^{2+}/Ni^{4+} and Co^{3+}/Co^{4+} redox processes. Once the potential is higher than 4.5 V, Li^+ escapes from the material lattice and reacts with O^{2-} to form Li_2O, corresponding to the obvious plateau at 4.5 V in the initial charging process. It should be noted that only part of Li^+ can be embedded in the material in the initial discharge process; Li^+ and O^{2-} vacancies caused by Li_2O emerged from the electrode

Fig. 1 XRD patterns of $Li_{1.2}Mn_{0.54}Ni_{0.13}Co_{0.13}O_2$

Table 1 Lattice parameters of samples prepared with different chelating agents

	a(Å)	c(Å)	c/a	$I_{(003)}/I_{(104)}$	R-factor
GS	2.8477	14.2293	4.9948	1.6398	0.2692
PS	2.8462	14.2315	5.0000	1.4148	0.2790
CS	2.8486	14.2244	4.9934	2.0202	0.3002
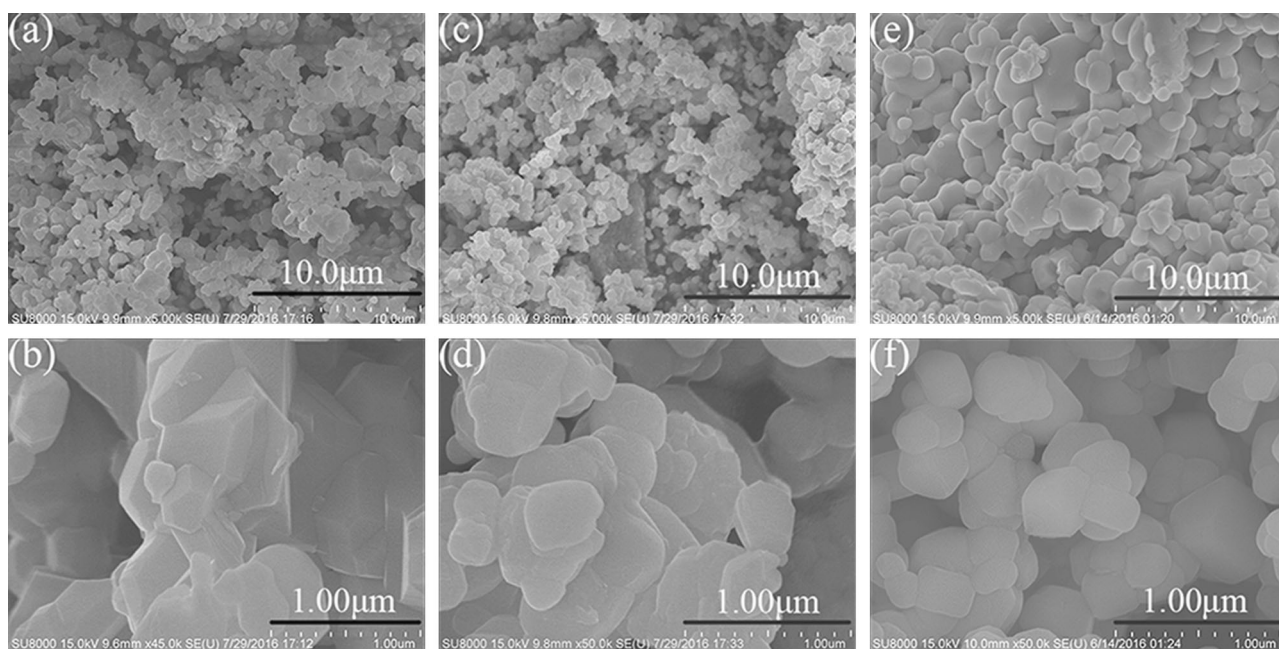
Fig. 2 SEM images of **a**, **b** CS sample; **c**, **d** GS sample; and **e**, **f** PS sample

material were occupied by metal ions partly. Owing to the disappearance of lattice vacancies, a part of Li^+ could not be embedded into the lattice, which causes the large irreversible capacity loss in the initial charge/discharge process [28–30].

The electrochemical tests are shown in Fig. 3. Figure 3a shows the initial charge and discharge curves of the sample prepared with different chelating agents. It can be seen that the initial discharge capacity of the samples prepared with PVP and citric acid is 231 and 207 mAh g^{-1}, respectively. The initial charge/discharge efficiencies of the samples prepared with citric acid, glycolic acid, and PVP were 70.4, 69.0, and 70.9%, respectively. Figure 3b is the rate performance of different materials. The capacity of CS and GS samples under low discharge rate is similar. When the discharge current reaches 1 C and above, the capacity of CS sample decreases rapidly, i.e., 38 mAh g^{-1} at 5 C, whereas the PS sample shows excellent rate performance with 99 mAh g^{-1} discharge capacity at 5 C. Therefore, PVP can improve the rate performance of the material, which is consistent with the previous XRD and SEM analysis.

Figure 4 shows the SEM images of materials synthesized with different chelating agents after 100 charge/discharge cycles. The samples' surface became unsmooth, and the particle size became bigger after cycles. The surface of the CS sample was the most rough of all and its particle size was the biggest, which corresponded to the worst cycle performance. The unsmooth surface may be caused by the dead lithium during charge and discharge cycles, which caused less available Li^+ for intercalation/deintercalation and capacity decay.

Figure 5a shows the cycle performance of the samples at a current of 1 C. It can be seen that the discharge capacity of CS sample under 1 C is the lowest and that of PS sample is the highest. After 100 cycles, the capacity of GS sample decreased from 150 to 138 mAh g^{-1}, with a high capacity retention of 91.7% compared with 70.4% for the PS sample. Therefore, glycolic acid as a chelating agent can improve the cyclic stability of the material, whereas PVP as a chelating agent can increase the discharge capacity of the material.

During the charge/discharge processes, besides the electrolytic decomposition, the internal resistance will be changed with the collapsed structure of the cathode material forming Li-dendrite, which results in increased dead lithium and decreased discharge capacity [31]. Charge/discharge profiles at 1 C of 2nd, 20th, 40th, 60th, 80th, and 100th cycles for $Li_{1.2}Mn_{0.54}Ni_{0.13}Co_{0.13}O_2$ samples prepared with glycolic acid and PVP are shown in Fig. 5. With the increase of the cycle number and the decrease of the discharge platform voltage, the charge and discharge capacity of the material decays gradually. The longer the discharge platform is, the greater the available capacity will be. The discharge platform of the PS sample decreased from 3.4–2.9 V to 3.1–2.4 V after100 cycles and that of the GS sample was from 3.4–2.7 V to 3.1–2.4 V. The above-mentioned phenomenon is known as the voltage decay of LMNCOs; it causes a reduced energy density and decreased capacity. This phenomenon may be caused by three reasons —activation of the Li_2MnO_3 component [32], phase transformation from layered structure to spinel-like structure [31, 33], and the polarization during cycles [34]. The initial

Fig. 3 a Initial charge/discharge curve of CS, GS, and PS samples; **b** rate performance of CS, GS, and PS samples
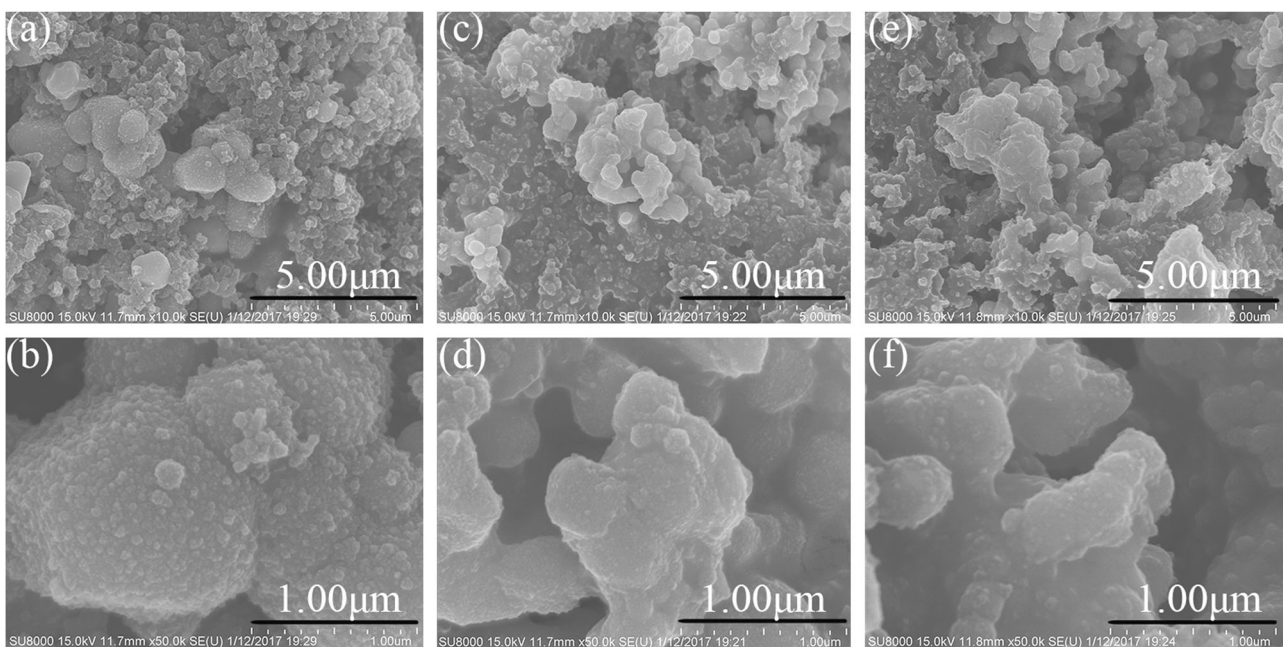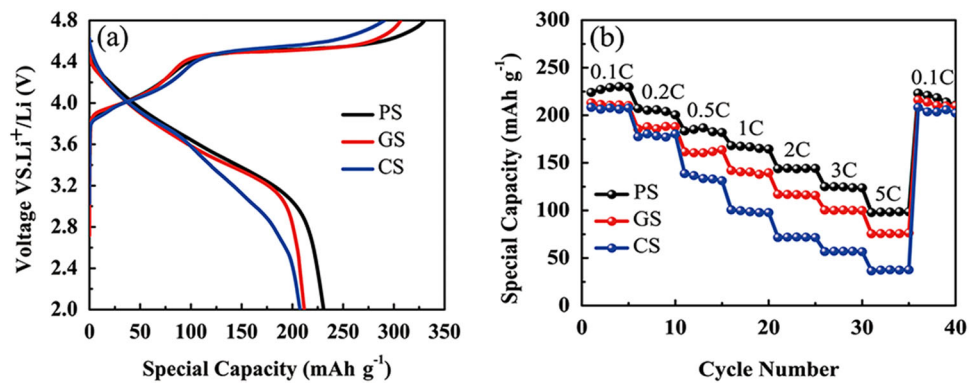

Fig. 4 SEM images of **a**, **b** CS sample; **c**, **d** GS sample; and **e**, **f** PS sample after 100 charge/discharge cycles

discharge platform of the PS sample was the highest, which means higher output power. However, with increasing cycles, the discharge platform voltage of PS sample dropped quickly, and the output power was decreased.

CV was carried out to explore the electrochemical redox responses of different $Li_{1.2}Mn_{0.54}Ni_{0.13}Co_{0.13}O_2$ electrodes. As shown in Fig. 6, all the cathode electrodes have two obvious anodic peaks at 4.0–4.3 V and 4.5–4.7 V in the initial anodic process. The first anodic peak could be attributed to the oxidation reactions of Ni^{2+} and Co^{3+}, which corresponds to the first voltage plateau during the initial charge/discharge process; the second anodic peak could be attributed to the lithium ion removal and simultaneous oxygen evolution, which is irreversible and corresponds to a large irreversible capacity thus leading to the disappearance of the second anodic peak during the following two scanning laps. In addition, a negative shift of the anodic peak potential was observed, which becomes smaller with the increase of scanning number, illustrating a good reversibility of the cathodes. It should be noted that there is still a little anodic peak at 4.5 V in the second cycle for CS sample, indicating that the CS sample was not fully activated in the first cycle to lead to a low efficiency during the second charge/discharge process. In the reversal scan, a distinct reduction in peak occurs at 3.3 V, corresponding to Mn^{4+} reduction to balance the charge of oxygen vacancies arising from the loss of oxygen in the initial charge process. The current peaks representing the reduction of Ni^{4+} and

Fig. 5 a Cycle performance of
CS, GS, and PS samples; **b**
charge/discharge profiles at 1 C
of 2nd, 20th, 40th, 60th, 80th,
and 100th cycles for GS sample;
c charge/discharge profiles at 1
C of 2nd, 20th, 40th, 60th, 80th,
and 100th cycles for PS sample
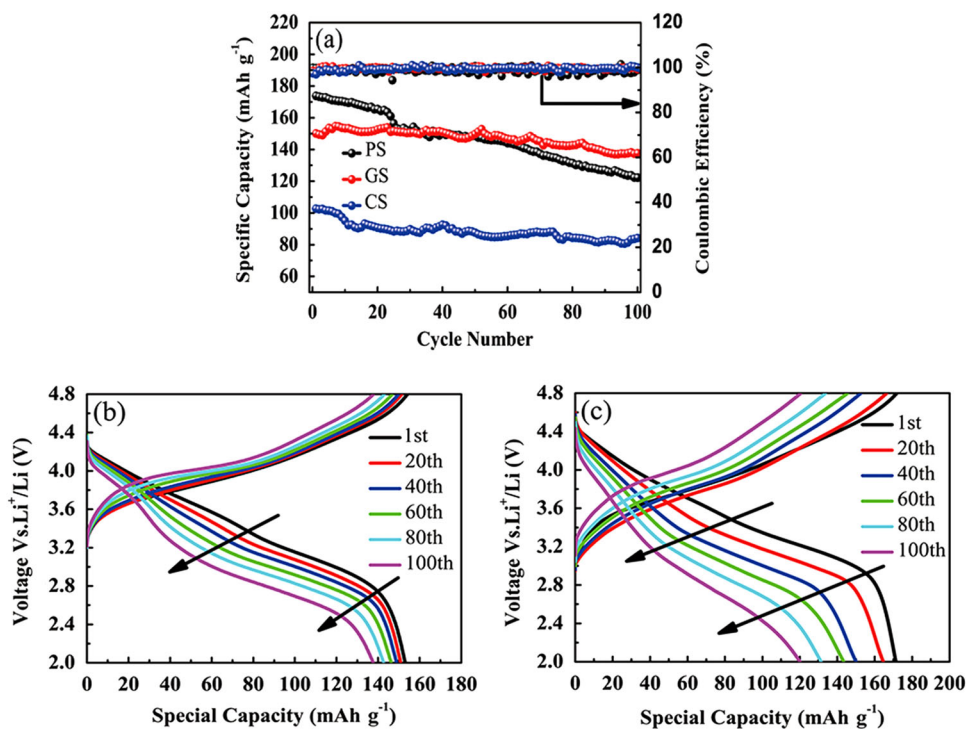
Fig. 6 CV curve of: **a** CS
sample, **b** GS sample, and **c** PS
sample
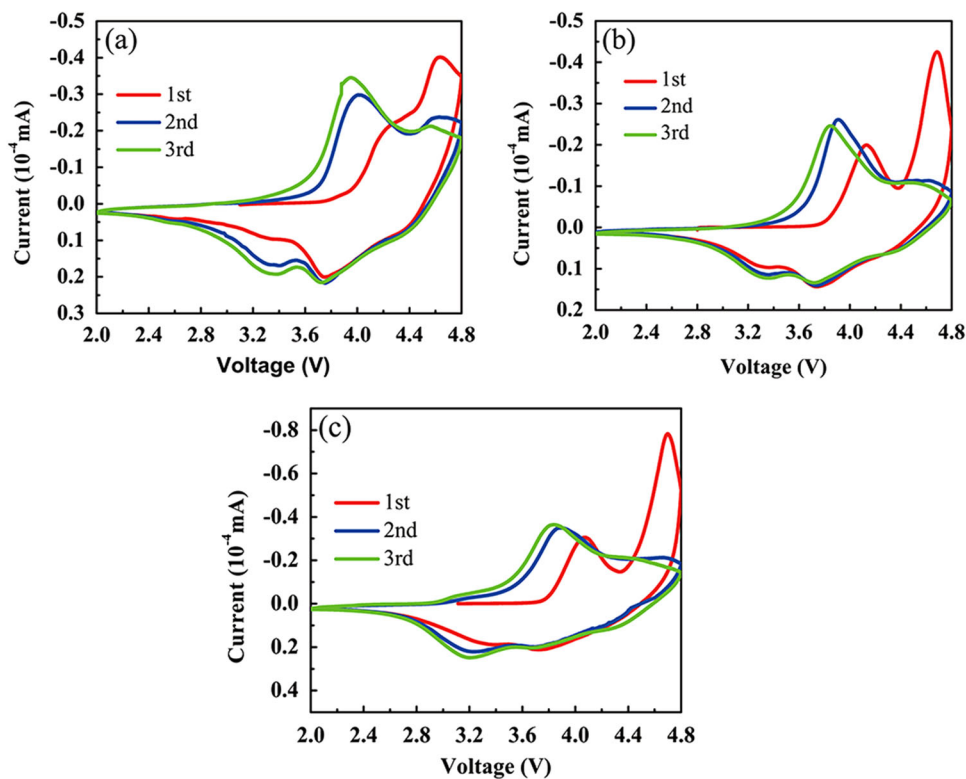
Co^{4+} were in the potential region of 3.6–4.4 V. The peak intensity of two cathodic peaks is increased as the scan continues, i.e., the cathodic peak is more obvious in the second and third cycle curves, indicating that the cathode material was further activated. These characteristics are consistent with the initial charge/discharge curves of the samples.

To investigate the kinetic processes of Li-ion intercalation/deintercalation for the Li-rich layered materials, EIS measurements were carried out. Figure 7 is the Nyquist plots of $Li_{1.2}Mn_{0.54}Ni_{0.13}Co_{0.13}O_2$ materials prepared with three different cleating agents. The impedance spectra of the Li-rich layered material generally contain several regions, reflecting the serial nature of Li-ion intercalation/deintercalation processes. Before the electrochemical inactivation of cells, the high-frequency region showing a semicircle is ascribed to Li-ion migration through the surface, the medium-frequency region is ascribed to charge-transfer reaction at the electrolyte-electrode interface, and the low-frequency region is ascribed to solid-state diffusion of lithium ions inside the intercalated compound [35]. The intercept of the high-frequency spectrum and the real part of the impedance diagram represent the ohmic resistance (R_s) of the solution. The semicircular diameter corresponds to the surface charge-transfer resistance (R_{ct}), followed by a slash which corresponds to the Warburg impedance of the lithium-ion diffusion. From Table 2, it could be seen that R_s of different samples could be ignored compared with R_{ct}, whereas R_{ct} (114.1 Ω) is the smallest for PS. The finding indicates that the ion's transmission channel of PS is short, which can accelerate the Li^+ deintercalation and thus it results in a good rate performance. The surface charge-transfer resistance of the PS sample is lower than that of the other two materials, corresponding to the highest rate of capability among the three materials.

From the above results, it could be concluded that the material prepared with PVP shows high initial discharge capacity and good rate performance and poor cycle performance. To enhance the cycle performance, graphene was coated on the PS sample. Figure 8 shows the cycle performance at 1 C rate of the pristine PS sample and the one coated with 3% graphene, namely Gr-PS. The capacities and capacity retention rates are shown in Table 3. The discharge capacity of the Gr-PS sample decreased from 162 to 145 mAh g^{-1}, with the capacity retention up to 89.8% after 100 cycles at a current of 1 C. The discharge capacity loss took place within the first 20 cycles, and the capacity retention of later 80 cycles was 95.4% (152–145 mAh g^{-1}). The improvement of the cycle performance could be attributed to graphene, which prevents the direct contact of the decomposition product HF of electrolyte with the active material. The HF could destroy the surface structure of active material to lead to the decrease in discharge capacity [36].
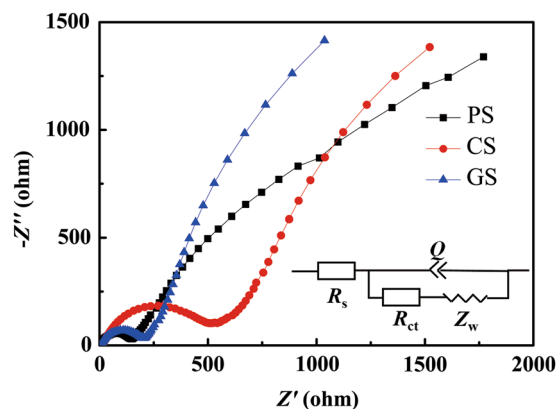

Fig. 7 Nyquist plots of PS, CS, and GS samples

Table 2 R_s and R_{ct} values of PS, CS, and GS samples

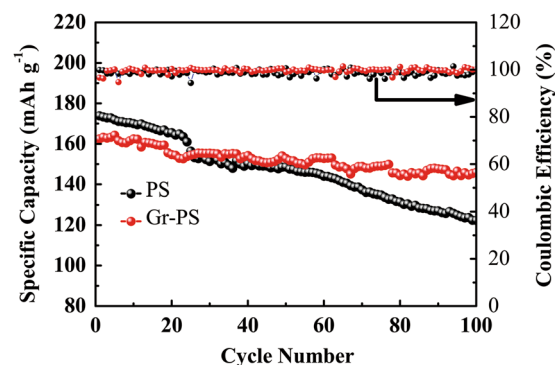| Sample	R_s (Ω)	R_{ct} (Ω)
PS	0.30	114.1
CS	11.98	454.1
GS	5.126	152.7

Fig. 8 Cycle performance of the PS and Gr-PS samples at 1 C rate

Table 3 The capacities and capacity retention rates of the PS, GS, and Gr-PS samples at 1 C rate

Samples	1st discharge capacity (mAh g^{-1})	100th discharge capacity (mAh g^{-1})	Capacity retention (%)
PS	174	122	70.4
GO-PS	163	146	89.8
GS	150	138	91.7

Figure 9 shows the Nyquist plots of the PS and Gr-PS samples after 100 cycles in discharge state, and the R_s and R_{ct} values are shown in Table 4. It can be seen that the value of R_s and R_{ct} increased after 100 cycles, and the value of R_s also could be ignored compared with that of R_{ct}. After
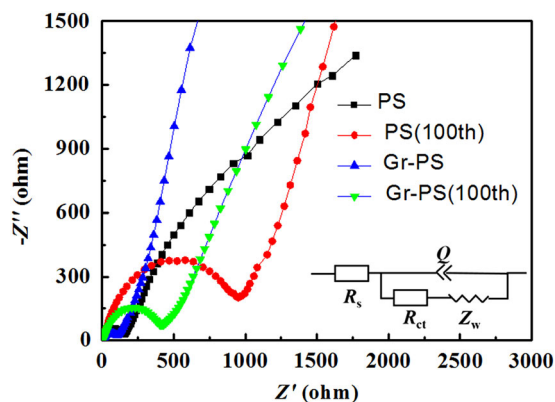
Fig. 9 Nyquist plots of the PS and Gr-PS samples

Table 4 R_s and R_{ct} values of the PS and Gr-PS samples

Sample	R_s (Ω)	R_{ct} (Ω)
PS	0.30	114.1
PS(100th)	12.82	697.1
Gr-PS	4.59	71.57
Gr-PS(100th)	8.01	364.1

coated with 3% grapheme, the R_{ct} value of PS sample was decreased to 71.57 Ω. The reduction of charge transfer resistance was due to the conductive property of graphite [37]. After 100 cycles, R_{ct} of the PS sample increased to 697.1 Ω, whereas that of the Gr-PS sample was just 364.1 Ω; so Gr-PS sample exhibits a better cycle performance.

4 Conclusion

Citric acid, glycolic acid, and PVP were used to synthesize Li-ion battery cathode material, $Li_{1.2}Mn_{0.54}Ni_{0.13}Co_{0.13}O_2$, by a sol–gel method. It was found that all the samples showed a α-NaFeO$_2$ structure with $R - \overline{3}m$ space group. In the case of PS, the material has the smallest particle size (200–350 nm) and the best rate performance and poor cycle stability. The PS sample has the highest initial discharge capacity (231 mAh g^{-1}) and the highest initial charge/discharge efficiency (70.9%). When glycolic acid was used, the sample displayed excellent cycle performance with the capacity retention rate of 91.7% after 100 cycles under 1 C current. EIS tests show that the CS sample showed the largest charge-transfer resistance (R_{ct}), whereas the PS sample showed the smallest R_{ct}, which could be responsible for its superior discharge capacity and rate performance. Coating with 3% graphene on the PS sample could improve the cycle performance, giving the capacity retention of up to 89.8% after 100 cycles at the current of 1 C.

Compliance with ethical standards

Conflict of interest The authors declare that they have no conflict of interest.

References

1. Goodenough JB (2012) Rechargeable batteries: challenges old and new. J Solid State Electrochem 16:2019–2029
2. Sivakumar P, Nayak PK, Grinblat J (2016) Effect of sonochemistry: Li-and Mn-rich layered high specific capacity cathode materials for Li-ion batteries. J Solid State Electrochem 20:1683–1695
3. Kang S, Li B, Qin H, Fang Y, Li X (2015) Simple solid-state method for synthesis of Li[Li$_{0.2}$0Mn$_{0.534}$Ni$_{0.133}$Co$_{0.133}$]O$_2$ cathode material with improved electrochemical performance in lithium-ion batteries. J Solid State Electrochem 19:525–531
4. Numata K, Sakaki C, Yamanaka S (1997) Synthesis of solid solutions in a system of LiCoO$_2$-Li$_2$MnO$_3$ for cathode materials of secondary lithium batteries. Chem Lett 1997:725–726
5. Thackeray MM, Kang SH, Johnson CS, Vaughey JT (2007) Li$_2$MnO$_3$-stabilized LiMO$_2$ (M=Mn, Ni, Co) electrodes for lithium-ion batteries. J Mater Chem 17:3112–3125
6. Xu H, Deng S, Chen G (2014) Improved electrochemical performance of Li$_{1.2}$Mn$_{0.54}$Ni$_{0.13}$Co$_{0.13}$O$_2$ by Mg doping for lithium ion battery cathode material. J Mater Chem A 2:15015–15021
7. Li Q, Li G, Fu C (2014) K$^+$-doped Li$_{1.2}$Mn$_{0.54}$Ni$_{0.13}$Co$_{0.13}$O$_2$: a novel cathode material with an enhanced cycling stability for lithium-ion batteries. ACS Appl Mater Inter 6:10330–10341
8. Nayak PK, Grinblat J, Levi M, Haik O (2015) Effect of Fe in suppressing the discharge voltage decay of high capacity Li-rich cathodes for Li-ion batteries. J Solid State Electrochem 19:2781–2792
9. Zhao Y, Xia M, Hu X (2015) Effects of Sn doping on the structural and electrochemical performance of Li$_{1.2}$Ni$_{0.2}$Mn$_{0.8}$O$_2$ Li-rich cathode materials. Electrochim Acta 174:1167–1174
10. Zhao J, Wang Z, Guo H (2015) Synthesis and electrochemical characterization of Zn-doped Li-rich layered Li[Li$_{0.2}$Mn$_{0.54}$Ni$_{0.13}$Co$_{0.13}$]O$_2$ cathode material. Ceram Int 41:11396–11401
11. Chen H, Hu Q, Huang Z (2016) Synthesis and electrochemical study of Zr-doped Li[Li$_{0.2}$Mn$_{0.54}$Ni$_{0.13}$Co$_{0.13}$]O$_2$ as cathode material for Li-ion battery. Ceram Int 42:263–269
12. Deng Y, Liu S, Liang X (2013) Study of carbon surface-modified Li[Li$_{0.2}$Mn$_{0.54}$Ni$_{0.13}$Co$_{0.13}$]O$_2$ for high-capacity lithium ion battery cathode. J Solid State Electrochem 17:1067–1075
13. Wise AM, Ban C, Weker JN (2015) Effect of Al$_2$O$_3$ coating on stabilizing LiNi$_{0.4}$Mn$_{0.4}$Co$_{0.2}$O$_2$ cathodes. Chem Mater 27:6146–6154
14. Yuan W, Zhang HZ, Liu Q, Li GR (2014) Surface modification of Li(Li$_{0.17}$Ni$_{0.2}$Co$_{0.05}$Mn$_{0.58}$)O$_2$ with CeO$_2$ as cathode material for Li-ion batteries. Electrochim Acta 135:199–207
15. Sun S, Wan N, Wu Q (2015) Surface-modified Li[Li$_{0.2}$Ni$_{0.17}$Co$_{0.07}$Mn$_{0.56}$]O$_2$ nanoparticles with MgF$_2$ as cathode for Li-ion battery. Solid State Ionics 278:85–90
16. Lu C, Wu H, Chen B (2015) Improving the electrochemical performance of Li$_{1.2}$Mn$_{0.52}$Co$_{0.08}$Ni$_{0.2}$O$_2$ cathode material by uniform surface nanocoating with samarium fluoride through depositional-hydrothermal route. J Alloy Compd 634:75–82

17. Zhou L, Zhao D, Lou XW (2012) $LiNi_{0.5}Mn_{1.5}O_4$ hollow structures as high-performance cathodes for lithium-ion batteries. Angew Chem 124:243–245

18. Zhao C, Shen Q (2014) Organic acid assisted solid-state synthesis of $Li_{1.2}Ni_{0.16}Co_{0.08}Mn_{0.56}O_2$ nanoparticles as lithium ion battery cathodes. Curr Appl Phys 14:1849–1853

19. Bhuvaneswari D, Kalaiselvi N (2012) Surfactant-coassisted sol-gel synthesis to prepare $LiNi_yMn_yCo_{1-2y}O_2$ with improved electrochemical behavior. J Solid State Electrochem 16:3667–3674

20. Shi SJ, Tu JP, Tang YY (2013) Combustion synthesis and electrochemical performance of $Li[Li_{0.2}Mn_{0.54}Ni_{0.13}Co_{0.13}]O_2$ with improved rate capability. J Power Sources 228:14–23

21. Zhang L, Wu BR, Li N, Wu F (2014) Hierarchically porous micro-rod lithium-rich cathode material $Li_{1.2}Ni_{0.13}Mn_{0.54}Co_{0.13}O_2$ for high performance lithium-ion batteries. Electrochim Acta 118:67–74

22. Li Y, Mei J, Guo X (2016) Hollow $Li_{1.2}Mn_{0.54}Ni_{0.13}Co_{0.13}O_2$ micro-spheres synthesized by a co-precipitation method as a high-performance cathode material for Li-ion batteries. RSC Adv 6:70091–70098

23. Feinle A, Elsaesser MS, Hüsing N (2016) Sol-gel synthesis of monolithic materials with hierarchical porosity. Chem Soc Rev 45:3377–3399

24. Abuzeid HAM, Hashem AMA, Abdel-Ghany AE (2011) De-intercalation of $Li_xCo_{0.8}Mn_{0.2}O_2$: a magnetic approach. J Power Sources 196:6440–6448

25. Myung ST, Kumagai N, Komaba S (2001) Effects of Al doping on the microstructure of $LiCoO_2$ cathode materials. Solid State Ionics 139:47–56

26. Jiao LF, Zhang M, Yuan HT (2007) Effect of Cr doping on the structural, electrochemical performance of $Li[Li_{0.2}Ni_{0.2-x/2}Mn_{0.6-x/2}Cr_x]O_2$ (x=0, 0.02, 0.04, 0.06, 0.08) as cathode materials for lithium secondary batteries. J Power Sources 167:178–184

27. Dahn JR, Sacken von U, Michal CA (1990) Structure and electrochemistry of $Li_{1\pm y}NiO_2$ and a new Li_2NiO_2 phase with the $Ni(OH)_2$ structure. Solid State Ionics 44:87–97

28. Nadimpalli SPV, Sethuraman VA, Abraham DP (2015) Stress evolution in lithium-ion composite electrodes during electrochemical cycling and resulting internal pressures on the cell casing. J Electrochem Soc 162:A2656–A2663

29. Ren S, Chen R, Maawad E (2015) Improved voltage and cycling for Li^+ intercalation in high-capacity disordered oxyfluoride cathodes. Adv Sci 2:1500128

30. Croy JR, Gallagher KG, Balasubramanian M (2014) Quantifying hysteresis and voltage fade in $xLi_2MnO_3 \cdot (1-x)LiMn_{0.5}Ni_{0.5}O_2$ electrodes as a function of Li_2MnO_3 content. J Electrochem Soc 161:A318–A325

31. Mohanty D, Li J, Abraham DP (2014) Unraveling the voltage-fade mechanism in high-energy-density lithium-ion batteries: origin of the tetrahedral cations for spinel conversion. Chem Mater 26:6272–6280

32. Yu SH, Yoon T, Mun J (2013) Continuous activation of Li_2MnO_3 component upon cycling in $Li_{1.167}Ni_{0.233}Co_{0.100}Mn_{0.467}Mo_{0.033}O_2$ cathode material for lithium ion batteries. J Mater Chem A 1(8):2833–2839

33. Xu B, Fell CR, Chi M (2011) Identifying surface structural changes in layered Li-excess nickel manganese oxides in high voltage lithium ion batteries: a joint experimental and theoretical study. Energ Environ Sci 4(6):2223–2233

34. Croy JR, Kim D, Balasubramanian M (2012) Countering the voltage decay in high capacity $xLi_2MnO_3 \cdot (1-x)LiMO_2$ electrodes (M=Mn, Ni, Co) for Li^+-Ion batteries. J Electrochem Soc 159(6):A781–A790

35. Bai Y, Wang X, Zhang X (2013) The kinetics of Li-ion deintercalation in the Li-rich layered $Li_{1.12}[Ni_{0.5}Co_{0.2}Mn_{0.3}]_{0.89}O_2$ studied by electrochemical impedance spectroscopy and galvanostatic intermittent titration technique. Electrochim Acta 109:355–364

36. Hong J, Gwon H, Jung SK (2015) Review—lithium-excess layered cathodes for lithium rechargeable batteries. J Electrochem Soc 162:A2447–A2467

37. Jiang KC, Xin S, Lee JS (2012) Improved kinetics of $LiNi_{1/3}Mn_{1/3}Co_{1/3}O_2$ cathode material through reduced graphene oxide networks. Phys Chem Chem Phys 14(8):2934–2939